

Plateau moduli of Kremer-Grest models for commodity polymer melts

Carsten Svaneborg¹ and Ralf Everaers^{2, a)}

¹⁾*Department of Physics, Chemistry, and Pharmacy. University of Southern Denmark.*^{b)}

²⁾*ENSL, CNRS, Laboratoire de Physique (UMR 5672) and Centre Blaise Pascal de l'École Normale Supérieure de Lyon, F-69342 Lyon, France*

(Dated: 3 February 2026)

We estimate the plateau moduli of highly entangled end-pinned bead-spring polymer melts with $Z = 100$ and $Z = 200$ from the time-dependent elastic response to a step strain, which we first extrapolate to infinite time and then interpolate to zero strain. We present data for systems deformed in the melt state as well as for systems deformed at the primitive path level following the recent iPPA protocol. We observe excellent agreement between the plateau moduli obtained via the two deformation protocols and good agreement with the available experimental data for commodity polymer melts using a common mapping on the Kuhn scale.

^{a)}Electronic mail: ralf.everaers@ens-lyon.fr

^{b)}Electronic mail: zqex@sdu.dk

I. INTRODUCTION

Statistical theories of polymeric systems^{1–6} predict macroscopic properties based on a description and understanding of the microscopic structure and dynamics. Scientific progress in the field relies crucially on compilations of microscopic and macroscopic measurements for well-characterized samples. A classic example is the work by Fetters *et al.*⁷, who assembled for a wide range of commodity polymers rheological plateau moduli and chain dimensions inferred from scattering experiments.

Here we present a similar data set for a family of bead-spring model polymer melts^{8,9} which can be systematically mapped¹⁰ onto the polymer melts studied by Fetters *et al.*. Over the years, the microscopic structure and topology of these systems have been extremely well characterized^{8,11,12}. However, rheological measurements^{8,13–20} remain computationally challenging, because polymeric systems are soft and equilibrate slowly. Not only must care be taken in properly equilibrating samples²¹, but long runs and finite deformations are required to measure elastic responses with an acceptable signal-to-noise ratio^{22,23}. To make matters worse, the rapidly increasing relaxation times render studies of long chain melts difficult, which would otherwise help to reduce finite chain length effects or to better separate time or length scale. Here we combine several techniques to overcome the difficulties of the triple extrapolation to infinite chain length, infinite time and zero strain with the aim to obtain high quality estimates of the entanglement or plateau moduli $G_e = \rho k_B T / N_e$ and $G_N^{(0)} = \frac{4}{5} G_e$ ^{4,24}:

1. We use multi-scale relaxation methods to build well-equilibrated starting states without having to rely on brute-force equilibration^{25,26}. This allows us to study systems composed of chains measuring $Z = 100 – 200$ entanglement lengths and to essentially eliminate finite chain length effects.
2. We tether the chain ends to suppress equilibration modes like contour length fluctuations, reptation and constraint release^{4,16,24}. As a consequence, stress relaxation in deformed systems is limited to the rubber elastic plateau⁴.
3. We subject the samples to uni-axial elongations in the range of $0.7 \leq \lambda \leq 1.4$.
4. We infer the equilibrium normal stresses from well-controlled extrapolations to infinite

time of two independent sets of data obtained for samples strained either on the melt or the primitive path level²⁷.

5. Finally, we use the Mooney-Rivlin representation^{28,29} of the equilibrium stresses at finite deformations to infer the elastic response in the limit of vanishing strain.

The paper is structured as follows: in Sect. II we use Likhtman-McLeish theory to analyze how to estimate the plateau modulus from the elastic response of end-pinned melts strained in the melt state and discuss the behavior of melts strained at the primitive path level. In Sect. III we present the Kremer-Grest model and the systems we are studying, as well as the inverse primitive-path analysis method for straining systems at the primitive path level. In Sect. IV we present our results for the normal stress relaxation in systems deformed in the melt state and at the primitive path level along with the extrapolation of our data to infinite time and the interpolation of the results to zero strain. In Sect. V we compare our simulation results to experimental results and discuss how the configurational relaxation differs in systems deformed in the melt state and at the primitive path level. We finish with our conclusions in Sect. VI.

II. THEORY

We infer plateau moduli from the elastic response of long chain model polymer melts with $Z = 100$ or 200 entanglements per chain. We measure this response in two different manners illustrated in Fig. 1:

1. By subjecting our melts to a rapid uni-axial elongation and subsequently observing the decay of the normal tension in brute-force simulations of the physical relaxation dynamics.
2. By converting our melts to the corresponding primitive path meshes¹¹, straining the primitive path meshes, reverting back to the full Kremer-Grest interactions, and equilibrating the resulting conformation²⁷.

Below we discuss the expected time evolution of the normal stresses during the brute-force simulations and the final equilibration phase of the primitive path accelerated relaxation.

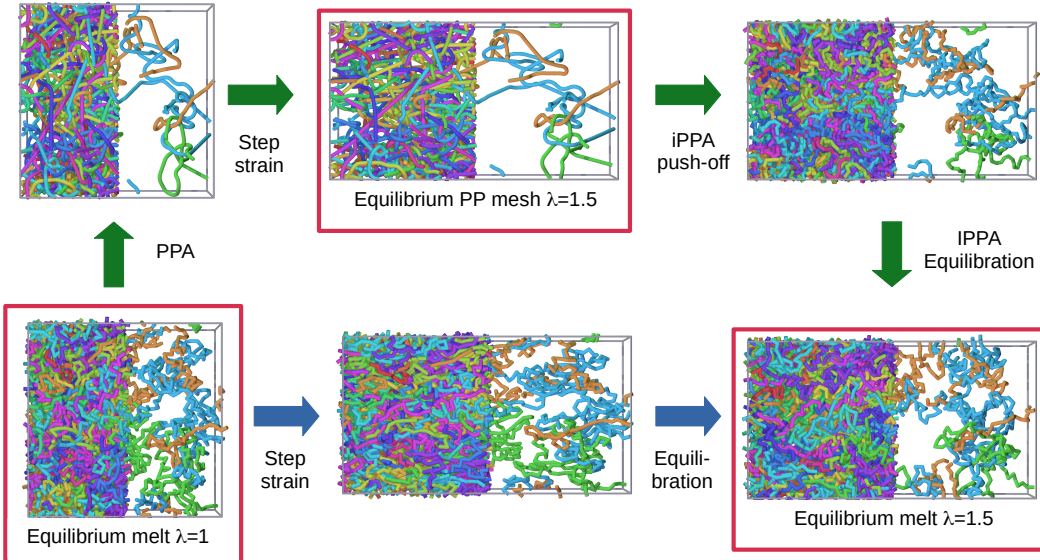


FIG. 1. Illustration of the present methodology. The tiny system visualized here was designed for illustrative purposes only and comprise $M = 30$ chains with $Z = 3$ entanglements. In each visualization the left side shows the whole melt, and the right side only the same three representative chains. We use two methods for stress relaxation: brute force (blue arrows, bottom row) and primitive-path acceleration (green arrows, top row). The brute force approach starts with an unstrained melt state (bottom left), which is rapidly step strained (bottom center), and followed by a very long stress relaxation at constant strain simulation (bottom right). The primitive path accelerated method start by generating the equivalent primitive path mesh (top left), the mesh is step strained and equilibrated (top center). An inverse PPA push-off is performed whereby excess contour length is reintroduced while switching back to the KG force field (top right). The resulting (unphysical) conformation is equilibrated in a relatively short constant strain simulation.

A. Shear relaxation modulus for polymer melts with end-pinned chains

The stress relaxation dynamics of a melt with pinned chain ends can be written as a limit of the Likhtman-McLeish theory²⁴

$$\frac{G(t)}{G_e} = \frac{4}{5} + \frac{1}{5Z} \sum_{p=1}^{Z-1} \exp\left(-\frac{p^2 t}{\tau_R}\right) + \frac{1}{Z} \sum_{p=Z}^{N_K} \exp\left(-\frac{2p^2 t}{\tau_R}\right). \quad (1)$$

where we have eliminated the terms describing stress relaxation via contour length fluctuations, reptation and constraint release. Here N_K denotes the number of Kuhn segments in the polymer, $Z = N_K/N_{eK}$ the number of entanglements per chain, N_{eK} the number of Kuhn segments between entanglements,

$$G_e = \frac{\rho_K k_B T}{N_{eK}} \quad (2)$$

the entanglement modulus, $\tau_R = N_K^2 \tau_K$ the Rouse time, $\tau_e = N_{eK}^2 \tau_K$ the entanglement time, τ_K the microscopic Kuhn time^{10,12}, and ρ_K the number density of Kuhn segments. Assuming $N_K \gg Z \gg 1$ one can replace the discrete sums in Eq. 1 by integrals. Using $\text{erfc}[x]$ to denote the complementary error function, the resulting approximation

$$\begin{aligned} \frac{G(t)}{G_e} = & \frac{4}{5} \left(1 - \frac{1}{Z} \right) + \frac{1}{5} \frac{\sqrt{\pi}}{2} \sqrt{\frac{\tau_e}{t}} \text{erfc} \left(\frac{1}{2} \sqrt{\frac{t}{\tau_R}} \right) \\ & + \sqrt{\frac{\pi}{8}} \sqrt{\frac{\tau_e}{t}} \exp \left(-\frac{2t}{\tau_e} \right) \end{aligned} \quad (3)$$

is valid for times $t \gg \tau_K$.

Up to the entanglement time, τ_e , the shear relaxation modulus, $G(t)$, is dominated by the last term in Eqs. (1) and (3), which describes the Rouse relaxation of short wavelength modes not affected by entanglements. This contribution reduces to zero beyond the entanglement time, τ_e . At the entanglement time, τ_e , $G(t)$ has decayed to a value of the order of the entanglement modulus, G_e , defined in Eq. (2). The second term describes the relaxation of $1/5$ of the remaining stress over the Rouse time, τ_R , via the equilibration of longitudinal tension along the tube²⁴. For times $\tau_e \ll t \ll \tau_R$ the argument of the complementary error function is small and $\text{erfc}[x] \approx 1 - 2x/\sqrt{\pi}$, so that Eq. 3 reduces to

$$\frac{G(t)}{G_e} = \frac{4}{5} \left(1 - \frac{1}{Z} \right) + \frac{1}{5} \left[\frac{\sqrt{\pi}}{2} \sqrt{\frac{\tau_e}{t}} - \frac{1}{2Z} \right]. \quad (4)$$

Eq. (4) thus suggest two different protocols for estimating plateau moduli from the elastic response to a step strain. If the stress relaxation can be followed to completion over times $\tau_R \ll t$, $G_N^{(0)}$ can be read off directly as

$$\lim_{t \rightarrow \infty} G(t) = G_N^{(0)} = \frac{4}{5} \left(1 - \frac{1}{Z} \right) G_e \quad (5)$$

for pinned chain ends with the plateau modulus asymptotically decaying to $4/5$ of the entanglement modulus⁴.

If the stress relaxation can only be followed into the plateau regime, then Eq. (4) suggests that data for $G(t)$ from the range $\tau_e \ll t \ll \tau_R$ extrapolate to an apparent plateau modulus, $G_N^{(0,app)}$, when plotted as a function of $1/\sqrt{t}$:

$$G(t) = G_N^{(0,app)} + \frac{\sqrt{\pi}}{10} \sqrt{\frac{\tau_e}{t}} G_e \quad (6)$$

$$G_N^{(0,app)} = G_N^{(0)} - \frac{1}{10Z} G_e \quad (7)$$

For computational studies this second route has considerable merit, since $\tau_R = Z^2 \tau_e$ can exceed the entanglement time by orders of magnitude for highly entangled chains with $Z \gg 1$. In particular, the finite chain-length corrections to the asymptotic relation $G_N^{(0)} = G_N^{(0,app)} = \frac{4}{5} G_e$ can be made arbitrarily small for larger Z without the need to extend the length of the simulations farther and farther beyond the entanglement time.

B. Stress relaxation in melts deformed at the primitive path level

As an alternative and potentially faster route towards the equilibrated strained state²⁷, we have (i) used Primitive Path Analysis (PPA)¹¹ to convert our end-pinned melts into topologically equivalent meshes of primitive paths, (ii) deformed the latter at zero temperature (i.e. by continuously minimizing the energy in the course of the deformation), and (iii) reverted the interactions and temperature back to the original force field and the reference temperature (for details on the implementation see Ref.²⁷ and Sec. ???). Importantly, as in the brute-force simulations of the physical dynamics, the microscopic topological state of the melts is preserved during the entire procedure. To sketch an argument comparable in form to the theory in Sec. II A, below we first discuss the effect of PPA on the chain conformations in mode space. In a second step, we consider the evolution of the chain conformations in unstrained samples during the equilibration after switching back to the full KG force field. In the final step, we consider the normal stresses during this equilibration for systems that were strained on the primitive path level.

1. *From a polymer melt to a mesh of primitive paths*

PPA contracts the contour of the chains, $L_{pp} \ll L$, without significantly changing the chain statistics beyond the entanglement scale¹¹. In particular, the product of contour and

Kuhn length for the original chains, Ll_K , is equal to the product of contour and Kuhn length of the primitive paths, $L_{pp}a_{pp}$, as the mean-square end-to-end distance, $\langle R^2 \rangle$ remains unchanged. In mode space, the mean-square excitation $\langle x_p^2 \rangle$ of the p 'th Rouse mode for the chains in the melt⁴

$$\langle x_p^2 \rangle = \frac{k_B T}{k_p} \quad (8)$$

due to the equipartition theorem. Here k_p is the spring constant of the p 'th mode. During PPA it is reduced to^{30,31}

$$\langle X_p^2 \rangle = \gamma_p \frac{k_B T}{k_p} \quad (9)$$

for the randomly quenched³² primitive paths representing their average conformation [some Likhtman reference], while the fraction³⁰

$$\langle \delta x_p^2 \rangle = (1 - \gamma_p) \frac{k_B T}{k_p} . \quad (10)$$

of the mode amplitudes removed by PPA corresponds to the annealed fluctuations of the chains within their respective tubes. The fraction of quenched fluctuations in Eqs. (9) and (10) is given by²⁶

$$\gamma_p = \frac{4Z^2}{\pi^2 p^2 + 4Z^2} \quad (11)$$

and interpolates between $\gamma_p = 0$ for the eliminated short-wavelength modes ($p \gg Z$) and $\gamma_p = 1$ for the long-wavelength modes, which encode the preserved large scale structure ($p \ll Z$).

2. From a mesh of primitive paths to a polymer melt

After switching back to the original KG force-field the time evolution of $\delta x_p(t) = x_p(t) - X_p$ should be described by a Rouse-like dynamics with⁴

$$\delta x_p(t) = \delta x_p(0) e^{-t/\tau_p} + \int_0^t e^{-(t-t')/\tau_p} f_{xp}(t') dt' \quad (12)$$

where the amplitude of the random force f_{xp} is chosen such that Eq. (10) holds for times $t \gg \tau_p$. In particular, $\delta x_p(0) = 0$ and $x_p(0) = X_p$, since switching back to the original KG force-field only leads to a local buckling of the locally smooth primitive paths while the original contour length $L \gg L_{pp}$ is rapidly restored. Otherwise we expect the local fluctuations to recover as

$$\langle \delta x_p^2(t) \rangle = (1 - \gamma_p) \frac{k_B T}{k_p} (1 - e^{-2t/\tau_p}) . \quad (13)$$

3. From a strained mesh of primitive paths to a strained polymer melt

The same restoration of chain fluctuations inside the tube also occurs in samples, where the primitive path mesh has undergone a deformation (which below we take to be a shear deformation for notational simplicity). In particular, the shear stress in such a system can be written as the usual mode sum⁴

$$\sigma_{xy}(t) = \frac{\rho_K}{N_K} \sum_p k_p \langle x_p(t) y_p(t) \rangle \quad (14)$$

taking into account that a step shear at $t = 0$ transforms the chain coordinates as

$$\begin{aligned} x_p(0^+) &= x_p(0^-) + \gamma y_p(0^-) \\ y_p(0^+) &= y_p(0^-) \end{aligned}$$

and that for $t > 0$ the x - and y -coordinates evolve according to equations analogous to Eq. (12) with uncorrelated noise, $\langle f_{xp}(t) f_{yp}(t) \rangle = 0$. In particular, $\langle x_p(t) y_p(t) \rangle = \langle y_p^2(0^+) \rangle e^{-2t/\tau_p}$. Within the standard Rouse model ($\gamma_p = 0$), Eq. (14) reduces with⁴

$$G(t) = \frac{\sigma_{xy}(t)}{\gamma} = \frac{\rho_K k_B T}{N_K} \sum_p e^{-2t/\tau_p}$$

to the third term in Eq. (1). In the course of the primitive path accelerated relaxation procedure from Ref.²⁷, the shear deformation is only applied to the (quenched) primitive path mesh, so that $\langle x_p(t) y_p(t) \rangle = \langle Y_p^2 \rangle$ and

$$G(t) = \frac{\sigma_{xy}(t)}{\gamma} = \frac{\rho_K k_B T}{N_K} \sum_p \gamma_p. \quad (15)$$

It is instructive to compare Eq. (15) to Eq. (1). The latter describes the time-dependent elastic response to a step strain deforming the *instantaneous* chain conformations in a melt. In particular, the time-independent equilibrium response, Eq. (5), is directly observable only after the perturbed annealed parts of all modes have relaxed over their respective characteristic times. In contrast, straining the primitive path mesh in the iPPA protocol only affects the quenched *mean* excitations of the modes. In this case, Eq. (15) suggests that the time-independent equilibrium response should be observable almost immediately during the final equilibration phase. This might seem surprising given that the chain conformations are no less perturbed than in a strained melt, Eq. (13). The point is that no shear or normal stress are induced as long as the initial local buckling of the primitive paths and the subsequent rebuilding of the annealed fluctuations inside the tube are *isotropic*.

III. MODEL AND METHODS

A. The Kremer-Grest model

We simulate Kremer-Grest (KG) model^{8,33} polymer melts with an additional bending potential to control the chain stiffness^{9,34}. The KG polymer model³³ is a bead-spring model where beads interact via a Lennard-Jones potential truncated at $r_c = 2^{1/6}\sigma$. This Weeks-Chandler-Andersen³⁵ (WCA) potential has the functional form

$$U_{WCA}(r) = \begin{cases} 4\epsilon \left[\left(\frac{\sigma}{r}\right)^{12} - \left(\frac{\sigma}{r}\right)^6 + \frac{1}{4} \right] & r < r_c \\ 0 & r \geq r_c \end{cases} \quad (16)$$

Bonds are described by the FENE potential

$$U_{FENE}(r) = -\frac{kR^2}{2} \ln \left[1 - \frac{r^2}{R^2} \right]. \quad (17)$$

With the standard choices of $\epsilon = k_B T$, $R = 1.5\sigma$ and $k = 30\epsilon/\sigma^2$ the average bond length is given by $l_b = 0.965\sigma$. The chain stiffness is controlled by a bending potential

$$U(\Theta) = \kappa \epsilon (1 - \cos \Theta), \quad (18)$$

for the bond angle Θ , which allows to control the chain stiffness. The effect of the bending potential is parameterized by a dimensionless parameter κ , which controls the Kuhn length $l_K(\kappa)$ of our bead-spring chains^{12,26}. Here we present data for $\kappa \in [0 : 2.15]$ covering the values relevant to modelling commodity polymers¹⁰. To estimate $N_{eK}(\kappa)$ for our systems we use Eq. (60) of Ref.¹², for the bead friction $\zeta_b(\kappa)$ we use Eq. (27) of Ref.¹⁰, and for the Kuhn length $l_K(\kappa)$ we use Eq. (49) of Ref.²⁶ with $W = 1$. Together these relations provide an estimate $\tau_e(\kappa)$ as well as an estimate for the number of entanglements per chain Z given in Tables I and III.

Starting states for the simulated polymer melts with the standard bead density of $\rho_b = 0.85\sigma^{-3}$ were generated using a recently developed multiscale equilibration method²⁶. For integrating the Langevin dynamics of our systems, we used the Grønbech-Jensen/Farago (GJF) integration algorithm^{36,37} as implemented in the Large Atomic Molecular Massively Parallel Simulator (LAMMPS).^{38,39} The friction was set to $\Gamma_b = 0.5m_b\tau^{-1}$ and the dynamics integrated with a time step of $\Delta t = 0.01\tau$, where $\tau = \sigma\sqrt{m_b/\epsilon}$ is the LJ unit of time.

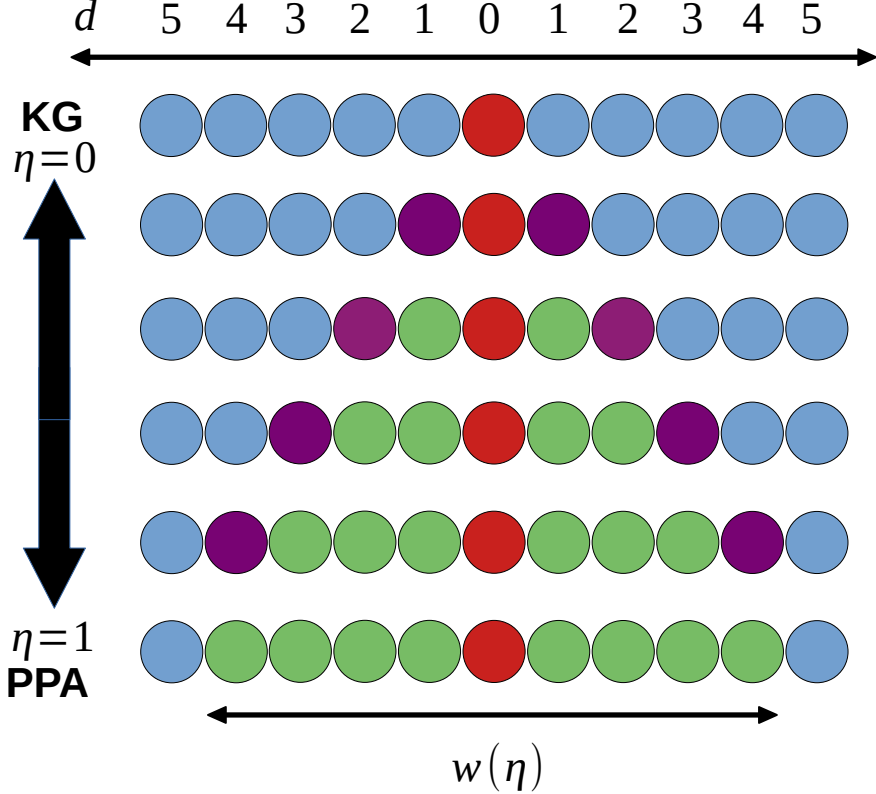


FIG. 2. Illustration of the step-wise transformation²⁷ between the KG and PPA force fields, which allows for a reversible interconversion between topologically equivalent melt states and primitive path meshes. The central red bead has WCA interactions with blue beads (KG, $\eta = 0$), no pair interactions with green beads (PPA, $\eta = 1$), and force capped interactions with magenta beads to switch WCA interactions on or off (iPPA, $0 < \eta < 1$). The PPA window in the illustration is $W = 4$, in PPA applications $W \propto \sqrt{N_{eK}}$.

B. Reversible switching between the KG and the PPA force fields

The primitive path analysis of the microscopic topological state of entangled polymers^{11,40} can be carried out with a variant of the Kremer-Grest force field, where non-bonded intra-chain interactions are disabled for pairs of beads within a PPA window $|i - j| \leq W \propto \sqrt{N_{eK}}$.

Switching from the KG to the PPA force field is unproblematic; for example, PPA can be implemented as an energy minimization starting directly from the original melt configuration. In contrast, using a PPA mesh as starting state for a simulation with the KG force field would not be numerically stable. Instead, one of us has developed the iPPA protocol (illustrated in Fig. 2) for a continuous force field transformation²⁷ that connects the full KG

TABLE I. Systems deformed in the melt state.

κ	Z	M	N_b	$\tau_e/10^3\tau$	$\tau_R/10^6\tau$
-1.0	100	510	11293	23	230
0.0	100	517	8408	13	130
0.0	200	1003	16819	13	540
1.0	100	553	4175	3.9	39
1.0	200	933	8352	3.9	160
2.0	100	451	1792	0.95	9.5
2.0	200	1044	3584	0.95	38

TABLE II. Plateau moduli and entanglement lengths extracted from simulations of systems deformed in the melt state.

κ	n_K	$G_N l_K^3/k_B T$
-1.0	2.27	0.0363 ± 0.0009
0.0	2.80	0.0684 ± 0.0025
1.0	4.69	0.2786 ± 0.0053
2.0	9.99	1.5429 ± 0.0247

force field (at $\eta = 0$) and the PPA force field (at $\eta = 1$) allowing for a reversible force-field transformation or "push-off"²¹, that is numerically stable and preserves topology. For detailed equations and characterization of the method, we refer to Ref.²⁷.

C. Deformation and brute-force relaxation of KG melts

For our first set of results the KG melts (see Table I) were subjected to volume-conserving uni-axial deformations, where they were deformed by a factor of $\lambda = 0.9$ or 1.1 in the parallel direction and by a factor of $1/\sqrt{\lambda}$ in the two perpendicular directions during simulations of $100\tau^{22,23}$. Subsequently, we performed a long stress relaxation simulation at constant deformation, where we have sampled at every time step all elements of the virial stress tensor $\sigma_{\alpha\beta}(t)$ to measure the time evolution of the normal stress

$$\sigma_n(t, \lambda) = \sigma_{xx}(t, \lambda) - 0.5 (\sigma_{yy}(t, \lambda) + \sigma_{zz}(t, \lambda)) . \quad (19)$$

TABLE III. Systems used for PP accelerated simulations, where the melts are deformed at the primitive path level. ($Z = 100$)

κ	M	N_b	n_K	$G_N l_K^3 / k_B T$
-1.00	510	11293	2.27	0.0394 ± 0.0007
-0.50	512	10157	2.45	0.0518 ± 0.0009
0.00	517	8408	2.80	0.0758 ± 0.0009
0.25	522	7338	3.08	0.0989 ± 0.0014
0.50	528	6237	3.47	0.1397 ± 0.0013
0.75	538	5155	3.99	0.2014 ± 0.0020
1.00	553	4175	4.69	0.3029 ± 0.0021
1.25	460	3347	5.60	0.4627 ± 0.0034
1.50	486	2679	6.76	0.7079 ± 0.0036
1.70	514	2261	7.90	0.9951 ± 0.0045
2.00	451	1792	9.99	1.6532 ± 0.0064
2.15	482	1617	11.23	2.1423 ± 0.0066

To deal with the strong fluctuations of the elements of the virial stress tensor, we have averaged $\sigma_{\alpha\beta}(t)$ over time intervals whose width is a multiple of the interval $[\tau_p, \tau_{p+1}]$ between the relaxation time of Rouse modes. With $\tau_p = \tau_K(N_K/p)^2$ these time intervals are equally spaced in representations, where data are plotted against $\sqrt{\tau_{relax}/t}$ for some suitable relaxation time τ_{relax} .

D. Inverse PPA of strained primitive path meshes

For our second set of results we carried out primitive path analysis (PPA) following the protocol described in Refs.^{11,12} for 12 melts with $Z = 100$ and $M \approx 500$ for a range of different values of $-1 \leq \kappa \leq 2.15$. Subsequently, we subjected the primitive path meshes to roughly 10 different uni-axial elongations over the range of $0.7 \leq \lambda \leq 1.4$. Since the contour length redistribution during these deformations occurs via energy minimization, it has a trivial computational cost.

We then used inverse primitive path analysis (iPPA)²⁷ as briefly described in Sec. III B

to convert the meshes back into topologically equivalent KG melt states. This was followed by a relaxation simulation of approximately $3 \times 10^4 \tau$ using the standard KG force field. The times t cited below are counted from the beginning of the last phase. In particular, we have again sampled the microscopic virial stress tensor during the process with the purpose of extrapolating the data to infinite time corresponding to an equilibrated strained melt.

E. Computational effort and efficiency

Comparing the computational effort of the brute force simulations and the primitive-path accelerated simulations the latter is significantly cheaper at a similar statistical accuracy. The PP push off requires 230τ of simulation time, followed by a relaxation simulation which were run for $10 - 50$ relaxation times. Thus we used simulations of $10000 - 50000\tau$ with a median of 32000τ independently of chain stiffness. The overhead of generating the PP mesh of the unstrained melt is amortised since all deformations starts from the same PP mesh.

For brute force stress relaxation, we performed simulations of $10 - 10^3 \tau_e$. The entanglement time depends strongly on chain stiffness with $\tau_e(\kappa = -1) = 23000\tau$, $\tau_e(\kappa = 0) = 13400\tau$, $\tau_e(\kappa = 1) = 3870\tau$, and $\tau_e(\kappa = 2) = 954\tau$. Hence stiffer melts are much cheaper to simulate compared to flexible melts. A meaningful comparison is to ask, if we invested the computational effort of a single PP accelerated simulation, how many τ_e of brute force relaxation would it produce. The result is 1.4, 2.4, 8.3, and 34 τ_e for $\kappa = -1, 0, 1, 2$, respectively. Thus our PP accelerated approach is orders of magnitude faster for the flexible systems, however the computational return is significantly diminished for the stiffer systems. The present paper comprises approximately $660K$ core hours or 76 CPU years of computational effort.

IV. RESULTS

A. Temporal evolution of the normal tension

In Fig. 3 we report data for the relaxation of the normal tensions $\sigma_n(t, \lambda)$ in deformed KG melts prepared via our two preparation protocols. For our present purposes, the most important observation is that the normal tensions appear to extrapolate to comparable values. Interestingly, they manifestly do so from different directions and possibly on different

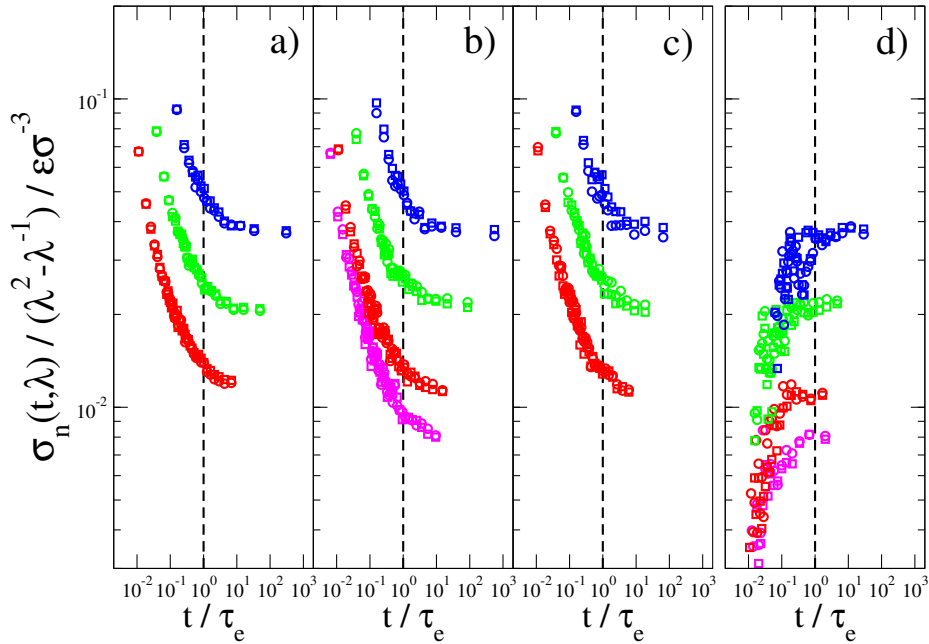


FIG. 3. Relaxation of normal tensions $\sigma_n(t, \lambda)$ in KG melts (a-c) after a volume-conserving uni-axial elongation of equilibrated KG melts by a factor of $\lambda = 1.1$, (d) after an iPPA pushoff following an equivalent deformation of corresponding primitive path meshes. Colors denote the chain stiffness of $\kappa = -1$ (magenta), $\kappa = 0$ (red), $\kappa = 1$ (green), and $\kappa = 2$ (blue). (a) $Z = 200$ and fixed chain ends, (b and d) $Z = 100$ and fixed chain ends, (c) $Z = 100$ and free chain ends. The vertical black dashed line illustrates the entanglement timescale τ_e .

time scales.

For systems strained in the melt state, the normal tensions exhibit the expected monotonous decay from a high initial value immediately after the step strain. In particular, the rubber elastic plateau is reached on the entanglement time, τ_e , while the stress relaxation in the initial Rouse regime is controlled by the Kuhn time, τ_K . As expected, we observe no discernible differences on the simulated time scales when comparing data for systems with $Z = 100$ and $Z = 200$ and for systems with fixed and free ends. With a Rouse time of $\tau_R/\tau_e = Z^2 = 10^4$ (4×10^4) for $Z = 100$ (200), it would take several orders of magnitude more computational work to reach the Rouse time for these systems.

In contrast, the normal tensions in melts derived via iPPA from strained primitive path meshes appear to reach a plateau after a relaxation time between $10^3\tau$ and τ_e and typically

faster than their homologues deformed in the melt state. Qualitatively, the observed behavior is in agreement with the theoretical arguments from Sec. II B. Note that in this case the normal stress *grows* in time instead of decreasing as in the case of systems deformed in the melt state. We tentatively interpret this as a gradual increase of the configurational temperature during the equilibration of the chain statistics, which translates into a reduced effective stiffness of the entropic springs.

B. Stress extrapolation to the limit of infinite time

Following the theoretical analysis in Sec. II, we have plotted the temporal evolution of the normal stresses in the plateaus as a function of $\sqrt{\tau_e/t}$ (Fig. 4). Contrary to our theoretical expectations, the normal tensions in melts deformed at the primitive path level do not become completely time-independent over the simulated time scales. Instead they vary over a range comparable to those expected and observed for systems deformed in the melt state. A post-analysis of our PP meshes revealed that the longitudinal tensions were not fully equilibrated, suggesting that in both cases a similar mechanism might be at the origin of the terminal stress relaxation.

We have fitted the data from both data sets to straight lines to estimate the normal stresses in the limit of infinite time,

$$\sigma_n(\lambda) = \lim_{t \rightarrow \infty} \sigma_n(t, \lambda) . \quad (20)$$

This extrapolation rests on solid theoretical grounds for systems deformed in the melt state and is plausible and supported by the data for those derived from deformed primitive path meshes.

To estimate the error of the resulting estimates of $\sigma_n(\lambda)$ we have focused on cases where we had at least two independent data sets. For the systems deformed in the melt state this is typically the case, because we have data for melts with $Z = 200$ and $Z = 100$ for identical values of κ . For the systems deformed at the primitive path level a significant fraction was elongated in two different directions. For all of these cases we have calculated the standard deviation of an ensemble of fits for the correlated data from individual relaxation runs where we varied the upper limit $\sqrt{\tau_e/t_{min}}$ for the retained data points over a factor of two and where we treated data for $\sigma_{ny}(t, \lambda) = \sigma_{xx}(t, \lambda) - \sigma_{yy}(t, \lambda)$ and $\sigma_{nz}(t, \lambda) = \sigma_{xx}(t, \lambda) - \sigma_{zz}(t, \lambda)$

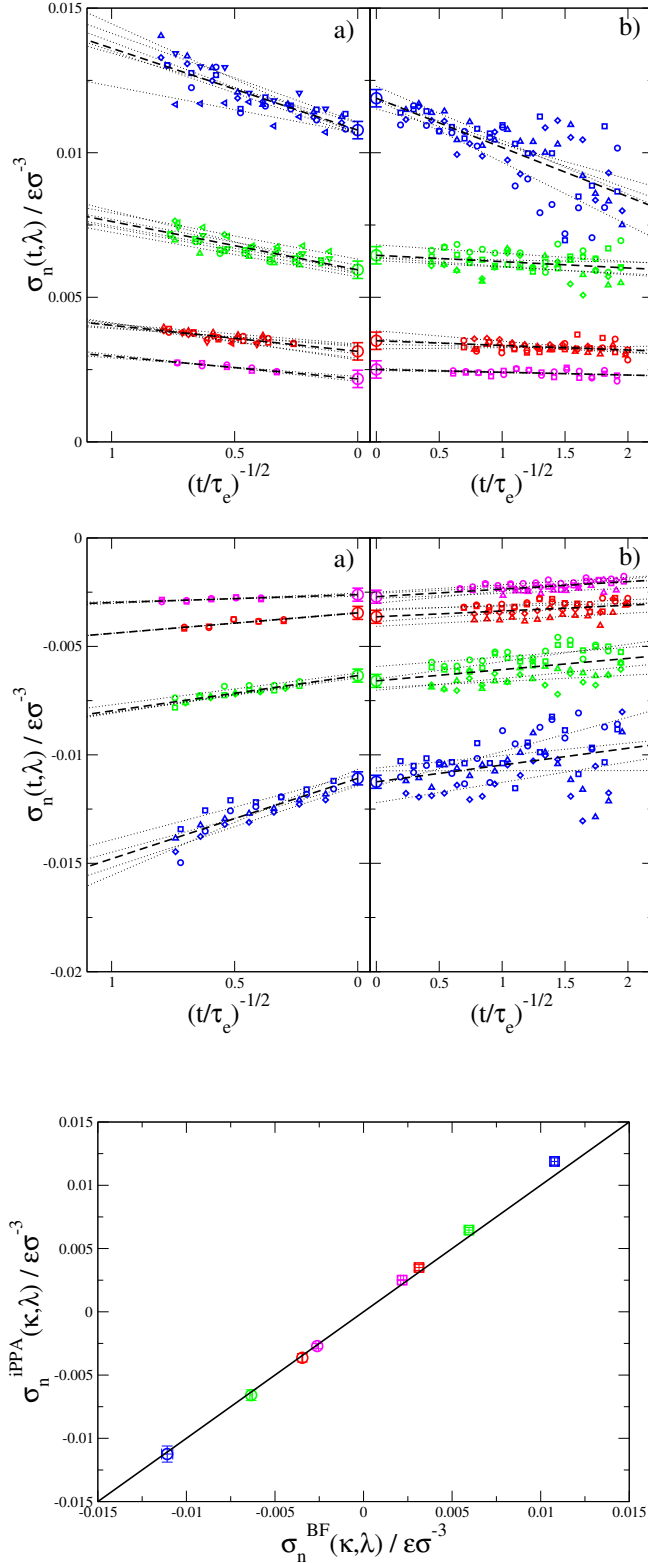


FIG. 4. Estimation of $G_N^{(0,app)}(\kappa, \lambda = 1.1)$ by extrapolation of the shear relaxation modulus from KG systems with $\kappa = -1$ (magenta, $*$), $\kappa = 0$ (red, box), $\kappa = 1$ (green, diamond), and $\kappa = 2$ (blue, triangle). (For details see the text)

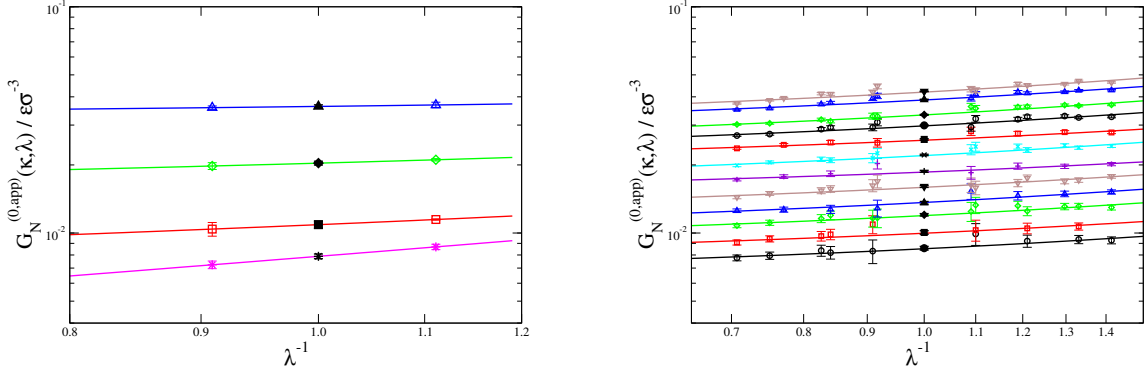


FIG. 5. Estimation of plateau moduli $G_N^{(0,app)}$ (black symbols at $\lambda = 1$) from extrapolations of symptotic normal stresses to zero strain via the Mooney-Rivlin form^{28,29,41}, Eq. (21). (a) systems deformed in the melt state with $\kappa = -1$ (magenta, *), $\kappa = 0$ (red, box), $\kappa = 1$ (green, diamond), and $\kappa = 2$ (blue, triangle). (b) systems deformed at the PP level with color denoting chain stiffness $\kappa = -1, -0.5, 0, 0.25, 0.5, 1, 1.25, 1.5, 1.7, 2, 2.15$ (bottom to top).

separately. For the iPPA data, the estimated errors did not show clear trends as a function of λ and κ and we combined the results into a combined estimated of $\delta_{\sigma_n} = 0.0003\epsilon/\sigma^3$ for data from an individual run. In the further analysis we divided these error by the square root of the number of independent data sets.

A comparison of the inferred asymptotic normal tensions for the two deformation protocols is shown in the bottom panel of Fig. 4. The good agreement suggests that our data can be trusted for the extraction of the plateau modulus.

C. Stress extrapolation to zero strain

We have used the Mooney-Rivlin form^{28,29,41}

$$G_N^{(0,app)}(\lambda) \equiv \frac{\sigma_n(\lambda)}{\lambda^2 - \lambda^{-1}} = 2C_1 + \frac{2C_2}{\lambda} \quad (21)$$

with

$$G_N^{(0,app)} = 2C_1 + 2C_2 \quad (22)$$

to extrapolate the asymptotic normal stresses to zero strain and to extract the estimates of the apparent plateau moduli listed in Tab. III

A pertinent question is how the plateau modulus is affected by the fact that we pin the chain ends. The junction affine model^{42–44} predicts the modulus of an equivalent system of phantom chains pinned by the ends. The reduced modulus is given by $G_X l_K^3 / (k_B T) = n_K / N_K$. For the present melts the modulus is roughly 1% of the obtained plateau moduli, which shows that pinning of the chain ends has a negligible effect on the plateau moduli.

The nearly stiffness independent slope of the fits suggests $2C_1/G_N \approx 0.75 \pm 0.04$ and $2C_2/G_N \approx 0.25 \pm 0.04$. The physical origin of the C_1 and C_2 terms have been discussed at length in the literature in the context of polymer networks see e.g. Ref.^{45,46}. Theories for rubber elasticity makes predictions for the parameters see e.g. Ref.⁴⁷ for a discussion. The consensus is that the modulus contribution due to the network structure is entirely described by the $2C_1$ parameter, whereas the entanglement contribution is distributed between the $2C_1$ and the $2C_2$ parameters. There is no consensus between the many theories on what this weighting should be. Nonetheless, the relatively large fraction of the modulus contributed by the C_1 parameter is surprising.

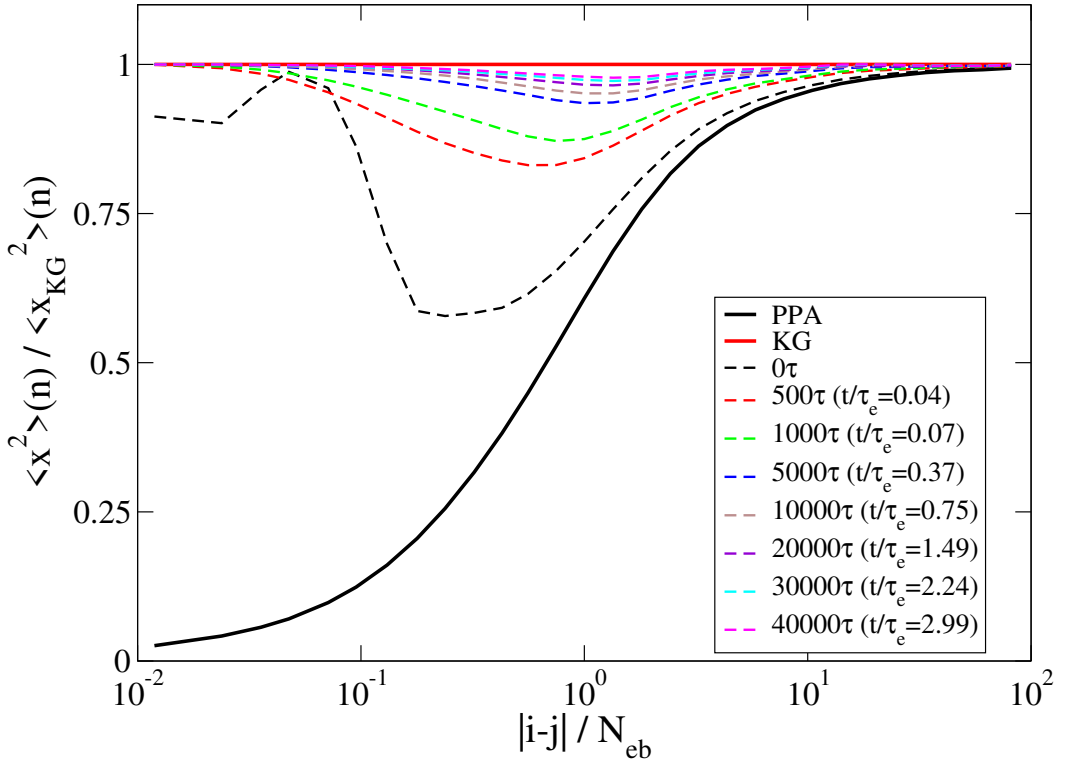


FIG. 6. Temporal evolution of the mean-square spatial distance $\langle x^2 \rangle(n)$ between monomers as a function of their distance $n = |i - j|$ along the chain during the equilibration following the iPPA pushoff for an undeformed melt with $Z = 100$ and $\kappa = 0$. Data are shown normalized to $\langle x^2 \rangle_{KG}(n)$ for equilibrated Kremer-Grest chains: Primitive-path mesh (solid black line), conformation just after the iPPA pushoff (black dashed line) and at different times during iPPA equilibration (colored dashed lines), fully equilibrated KG chains (solid red line).

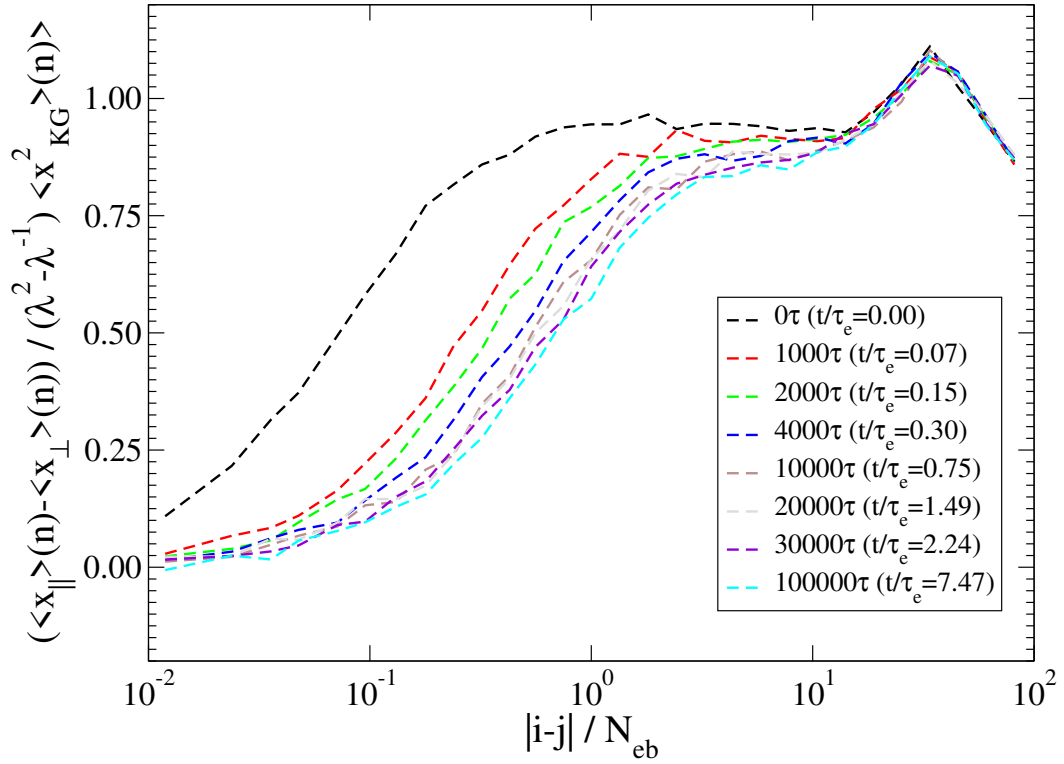


FIG. 7. Temporal evolution of the anisotropy $\left(\langle r_{||}^2 \rangle(n) - \langle r_{\perp}^2 \rangle(n) \right) / \left((\lambda^2 - 1/\lambda) \langle x^2 \rangle_{KG}(n) \right)$ of the mean-square spatial distances between monomers as a function of their distance $n = |i - j|$ along the chain for a melt with $Z = 100$ and $\kappa = 0$ that was strained in the melt state to $\lambda = 1.1$ with free ends (colored dashed lines).

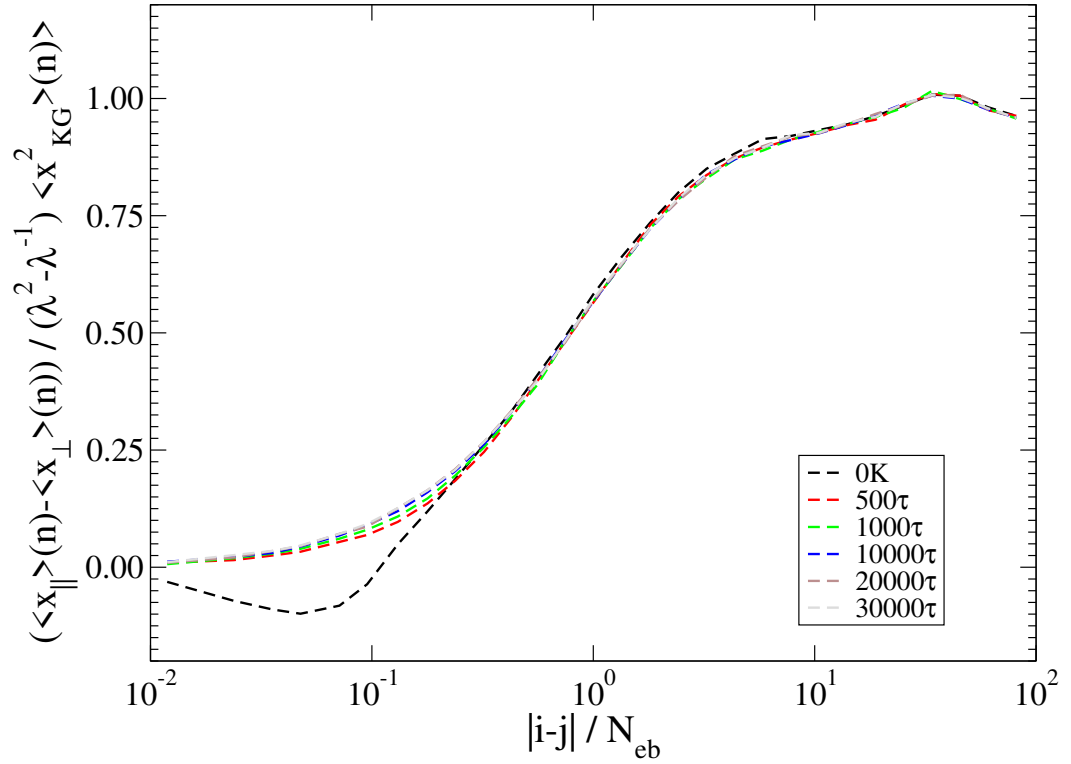


FIG. 8. Analogue of Fig. 7 for temporal evolution of the anisotropy of the chain conformations on different length scales during the iPPA equilibration after the primitive path mesh was strained to $\lambda = 1.5$.

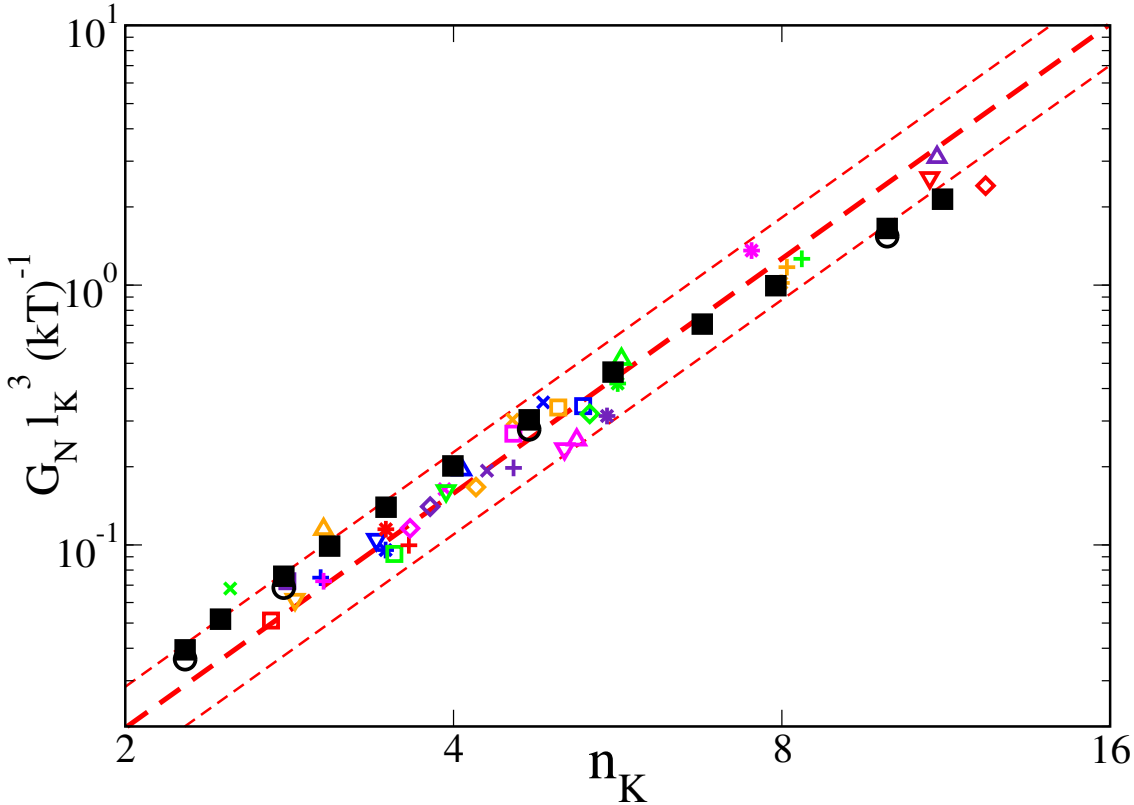


FIG. 9. Comparison between reduced plateau moduli from brute force simulations (big black circle), primitive-path accelerated simulations (black filled squares), and experimental data for (left to right) PI-50 (green \times), PI-7 (red \square), PDMS (violet \square), PI-20 (orange \triangledown), PI-34 (blue +), IPDMS (magenta +), Icis-PI (orange \triangle), cis-PBd (blue \triangledown), PIB(413) (blue *), cis-PI (red *), a-PP(463) (green \square), i-PP (red +), a-PP(413) (magenta \diamond), a-PP(348) (violet \diamond), a-PP (magenta \times), PIB (green \triangledown), a-PMMA (blue \triangle), i-PS (orange \diamond), a-PMA (violet \times), PI-75 (orange \times), PBd-20 (magenta \square), a-PS (violet +), PBd-98 (blue *), PEO (orange \square), POM (magenta \triangledown), a-PHMA (magenta \triangle), a-PVA (blue \square), SBR (green \diamond), P6N (violet *), a-P α MS (green *), a-PEA (green \triangle), PET (magenta *), s-PP (orange *), PE(413) (orange +), a-POA (green +), PC (red \triangledown), PE (violet \triangle), PTFE (red \diamond). For details regarding the polymer abbreviations see Ref.⁴⁸. The thick red dashed line indicates the predictions of the packing argument^{49,50} using $\alpha = 18$ and indicating a 20% error by the two thin dashed red lines.

V. DISCUSSION

A. Configurational relaxation and evolution of normal stresses for the two deformation protocols

The present simulations of long-chain end-pinned polymer melts over the time scale of $\mathcal{O}(10)$ entanglement times follow the equilibration of our systems over a fraction $\mathcal{O}(10)/Z^2 = \mathcal{O}(10^{-3})$ of their longest relaxation time. As a consequence, we are restricted to extrapolating normal tensions to the limit of infinite time, when ideally one would simply measure their equilibrium values. Extrapolations, even when based on a solid theoretical foundation as the one in Sec. II A, always require a leap of faith and it would be desirable to test their reliability by a comparison of data from independent approaches to the equilibrium state. As illustrated in Fig. 1 and independently of its computational efficiency, the iPPA protocol²⁷ provides us with the possibility to do just that.

How different are systems deformed in the melt state and at the primitive path level? To answer this question it is instructive to consider the temporal evolution of the configurational statistics on different length scales in the two cases. To set the stage, consider a solid, where macroscopic strain translates instantaneously all the way down to the scale of its constituent atoms or ions. As a consequence, their positions change affinely with the macroscopic shape and their distances multiply by the same factors of λ_α as the macroscopic dimensions of the sample. In particular, the present uniaxial elongations induce an asymmetry $(\langle r_{\parallel}^2 \rangle - \langle r_{\perp}^2 \rangle) / \langle r_{\alpha}^2 \rangle = (\lambda^2 - 1/\lambda)$ into distances, which were isotropic in the unstrained state, $\langle x^2 \rangle = \langle y^2 \rangle = \langle z^2 \rangle$. This asymmetry is at the origin of the observed normal tensions.

In a theoretical idealization the above affine deformation describes the situation in a polymer melt or a rubber-elastic solid immediately after an instantaneous step strain. In practice, the length scale dependent chain anisotropy shown in Fig. 7 always remains small on the bead scale, explaining why systems of this type can sustain large deformations without rupturing the (chemical) bonds along the polymer backbone. In particular, the figure shows how the subsequent internal rearrangements at the origin of the decay of the normal tension (Fig. 3) are associated with a gradual reduction of the chain anisotropy on and beyond the entanglement time and length scale.

In Fig. 8 we show corresponding data for the temporal evolution of the chain anisotropy

during the iPPA relaxation following a deformation of the primitive path mesh. The observed behavior is remarkably different as the asymmetry converges very quickly after the iPPA push-off, explaining why, as anticipated in Sec. II B, the observed normal tensions never exceed the asymptotic values and why they remain essentially constant while the overall chain statistics continue to undergo major changes (Fig. 6).

B. Comparison to experimentally measured plateau moduli

Simulation results for Kremer-Grest melts are most conveniently compared to experimental data using Kuhn units^{10,12} with the Kuhn length l_K as unit of length, the thermal energy $k_B T$ as unit of energy, and the Kuhn time τ_K (defined as the time required by a Kuhn segment to diffuse over a distance of l_K) as unit of time. In particular, a monodisperse polymer sample is characterized by two dimensionless numbers, the chain length $N_K = L/l_K$ expressed in units of Kuhn segments and the Kuhn number $n_K = l_K^3 \rho_K$ measuring density in units of Kuhn segments per Kuhn volume.

In Fig. 9 we report reduced plateau moduli, $G_N^{(0)} l_K^3 / k_B T$ as a function of the Kuhn number $n_K = l_K^3 \rho_K$ characterizing the melts. A first point to note is the excellent agreement between the moduli we have obtained for KG melts by deforming systems either in the melt state (○) or on the level of the primitive path mesh (■). Secondly, while in good agreement with the experimental data for commodity polymer melts⁵¹ over the entire relevant range of Kuhn numbers, our results exhibit less scatter. For small Kuhn numbers, our data are in good agreement with the prediction of the packing argument^{49,50} giving $N_{eK} = (\alpha/n_K)^2$, where α is the number of chains in the volume of a single entanglement. However, there are systematic deviations towards the upper end of the experimentally relevant range of Kuhn numbers, where the present results confirm our earlier PPA-based predictions^{10,12}.

VI. CONCLUSION

We have taken inspiration from the classic work by Fetters *et al.*⁷ to present data for the plateau moduli of a family of microscopically well characterized¹² bead-spring model polymer melts^{8,9} which can be systematically mapped¹⁰ onto the same commodity polymer melts. In a forthcoming paper, we will compare the rheological entanglement lengths⁵² inferred from

the present plateau moduli to measures of the entanglement length accessible via PPA¹¹ or Z⁵³ and test the latters' ability to predict the plateau modulus.

Compared to experiment, where rheological experiments preceded the microscopic sample characterization via neutron scattering by decades⁵⁴, the present results arrive decades after the microscopic structure and topology of Kremer-Grest melts was first investigated^{8,11}. If the computational results in Fig. 9 exhibit less scatter than the experimental data, then because the computational approach offers advantages in the preparation of monodisperse samples and in the determination of the microscopic chain dimensions.

The investigation of rheological properties remains computationally challenging, because polymeric systems are soft and equilibrate slowly. In particular, brute-force equilibration is much harder to circumvent for problems whose very nature is dynamics than for the equilibration of the static structure^{8,21,25,26,55-57}. The present results suggest that primitive-path accelerated stress relaxation²⁷ can at least play a useful role for the investigation of rubber-elastic systems under strain^{22,23,47,58,59}

VII. ACKNOWLEDGEMENT

We dedicate this work to Prof. Kurt Kremer on the occasion of his 70th birthday and the 40th anniversary of the publication of Ref.³³. It is our pleasure to acknowledge decades of stimulating discussions and interactions with Prof. Kremer and Dr. Grest on the present and related subjects.

The present simulations were performed by using the Large Atomic Massively Parallel Simulator^{38,39}(LAMMPS) Molecular Dynamics software. We acknowledge that part of the results of this research was obtained using the PRACE Research Infrastructure resource Joliot-Curie SKL based in France at GENCI@CEA. This work was partially supported by DeiC National HPC (g.a. DeiC-SDU-N5-2025141).

VIII. SUPPLEMENTARY MATERIAL

Plots of the evolution of chain statistics and anisotropy of the PP accelerated method for $\kappa = -1$ and $\kappa = 2$ are shown in the supplementary material,

IX. DATA AVAILABILITY

The melts studied here are a subset of those we have made available from Refs.^{60,61}. Our inverse PPA code has been implemented in the LAMMPS simulator^{38,39} and is documented in Ref.²⁷ and can be downloaded from Ref.⁶²

X. SUPPLEMENTARY MATERIAL

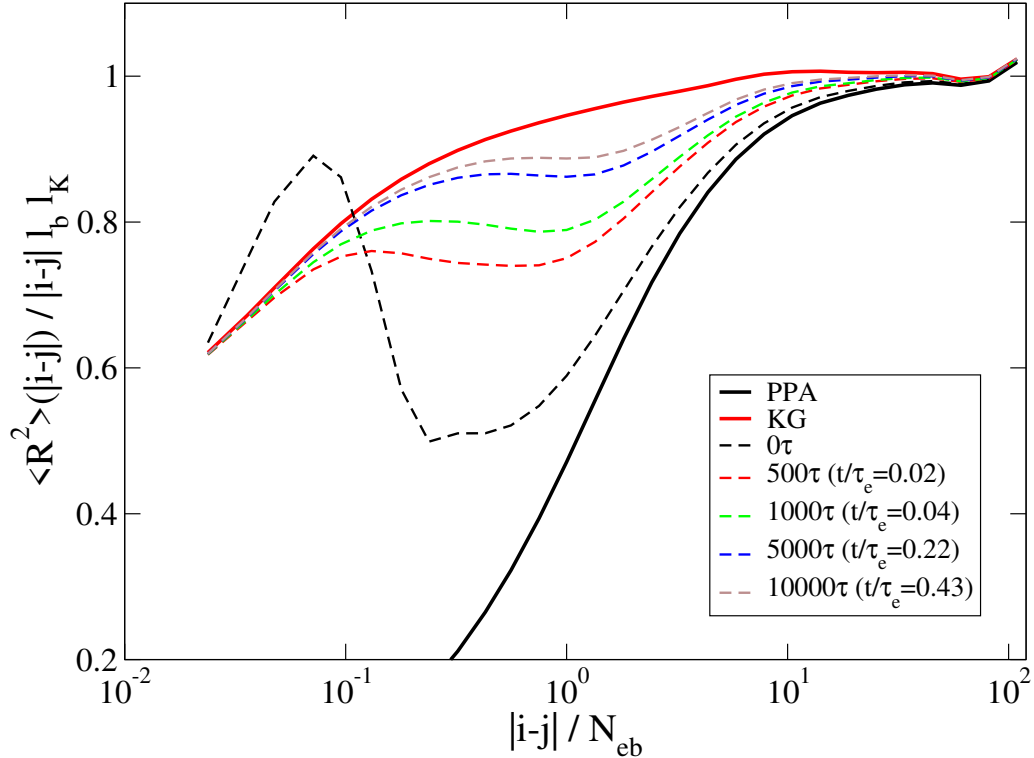


FIG. 10. Evolution of chain statistics during force field transformation and subsequent relaxation for a undeformed melt with $Z = 100$ and $\kappa = -1$. Initial KG conformation (solid red line), primitive-path mesh (solid black line), conformation just after thermalization (black dashed line) and subsequent relaxation (colored dashed lines).

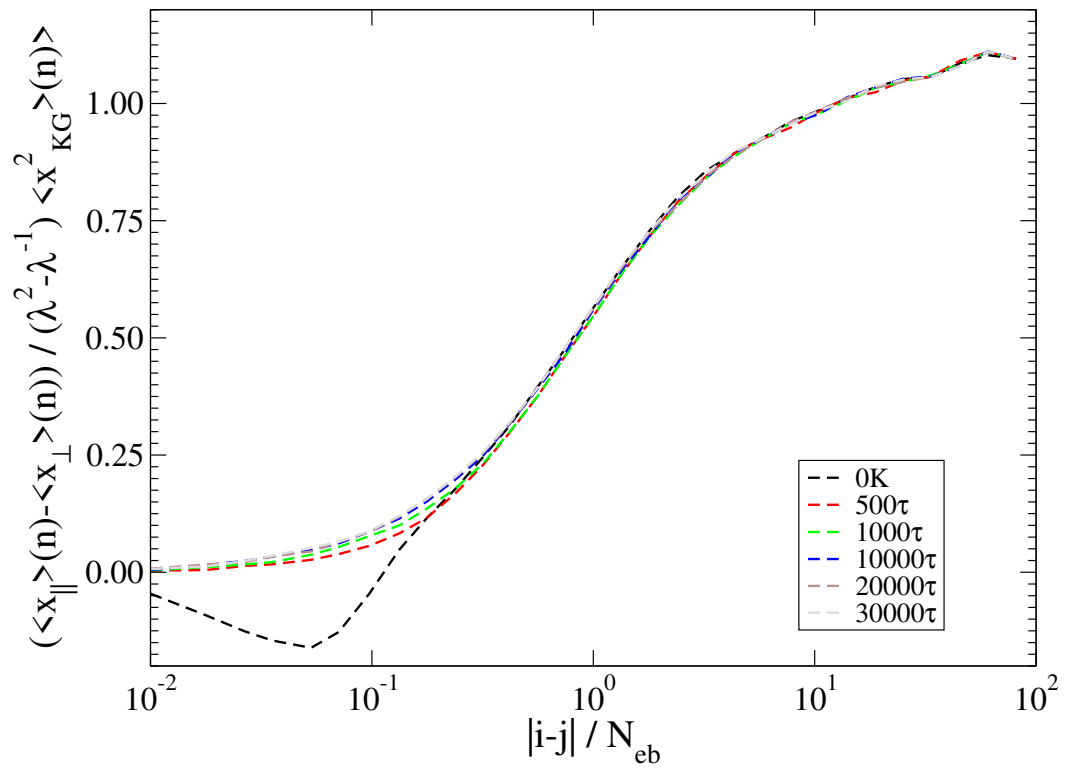


FIG. 11. Relaxation of the chain anisotropy after force field transformation for a melt with $Z = 100$ and $\kappa = -1$ strained at $\lambda = 1.5$.

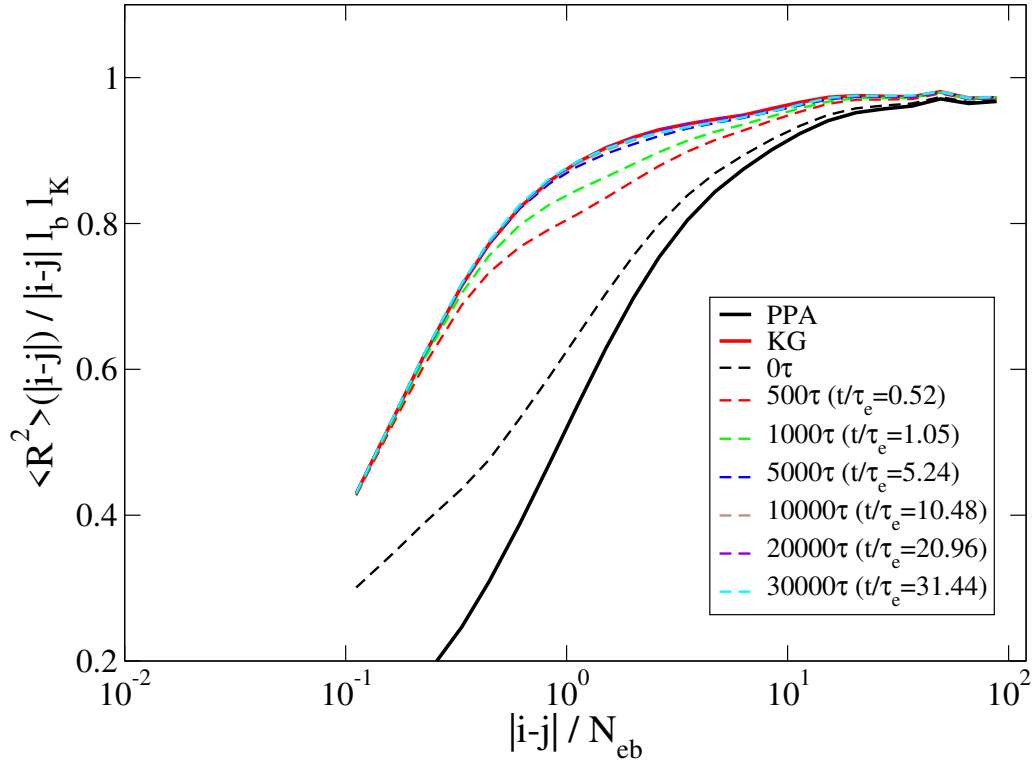


FIG. 12. Evolution of chain statistics during force field transformation and subsequent relaxation for a undeformed melt with $Z = 100$ and $\kappa = 2$. Initial KG conformation (solid red line), primitive-path mesh (solid black line), conformation just after thermalization (black dashed line) and subsequent relaxation (colored dashed lines).

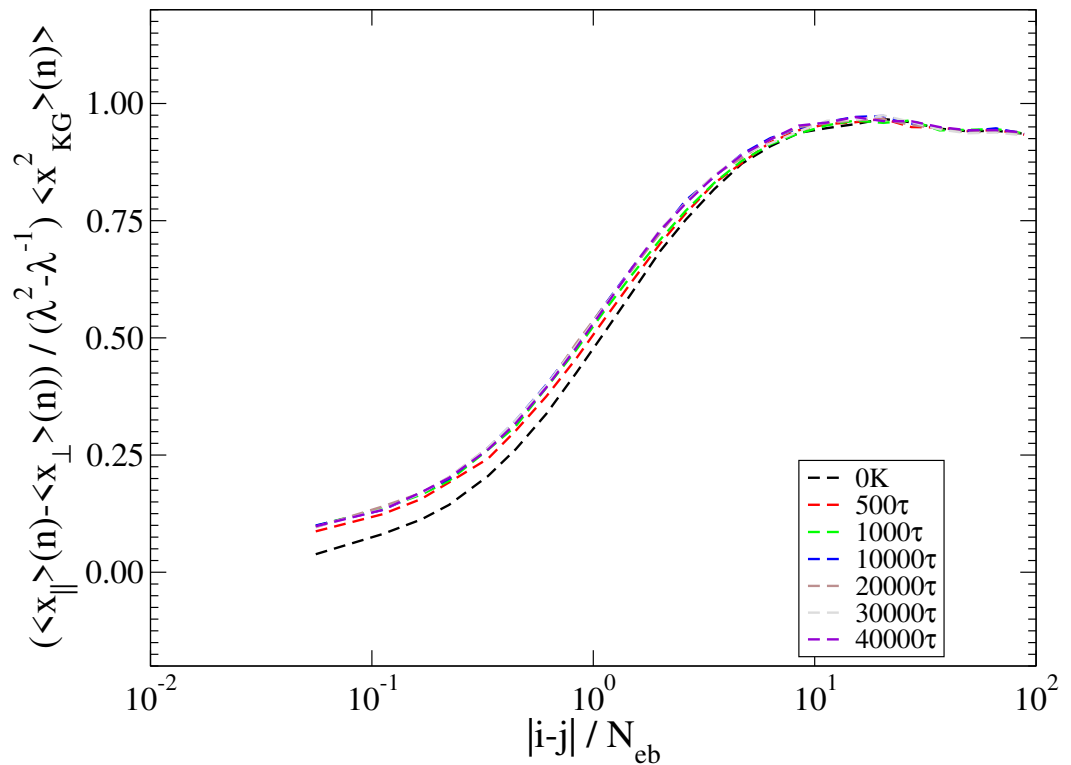


FIG. 13. Relaxation of the chain anisotropy after force field transformation for a melt with $Z = 100$ and $\kappa = 2$ strained at $\lambda = 1.5$.

REFERENCES

¹P. J. Flory, *Principles of polymer chemistry* (Cornell University Press, Ithaca N.Y, 1953).

²P. Flory and M. Volkenstein, “Statistical mechanics of chain molecules,” (1969).

³P. G. de Gennes, *Scaling Concepts in Polymer Physics* (Cornell University Press, Ithaca NY, 1979).

⁴M. Doi and S. F. Edwards, *The Theory of Polymer Dynamics* (Clarendon, Oxford, 1986).

⁵A. R. Khokhlov, A. Y. Grosberg, and V. S. Pande, *Statistical Physics of Macromolecules* (AIP-Press, Jericho NY, 1994).

⁶M. Rubinstein and R. H. Colby, *Polymer Physics* (Oxford University, New York, 2003).

⁷L. J. Fetters, D. J. Lohse, D. Richter, T. A. Witten, and A. Zirkel, “Connection between polymer molecular weight, density, chain dimensions, and melt viscoelastic properties,” *Macromolecules* **27**, 4639 (1994).

⁸K. Kremer and G. S. Grest, “Dynamics of entangled linear polymer melts: A molecular-dynamics simulation,” *J. Chem. Phys.* **92**, 5057 (1990).

⁹R. Faller, A. Kolb, and F. Müller-Plathe, “Local chain ordering in amorphous polymer melts: Influence of chain stiffness,” *Phys. Chem. Chem. Phys.* **1**, 2071 (1999).

¹⁰R. Everaers, H. A. Karimi-Varzaneh, F. Fleck, N. Hojdis, and C. Svaneborg, “Kremer-Grest models for commodity polymer melts: Linking theory, experiment, and simulation at the Kuhn scale,” *Macromolecules* **53**, 1901 (2020).

¹¹R. Everaers, S. K. Sukumaran, G. S. Grest, C. Svaneborg, A. Sivasubramanian, and K. Kremer, “Rheology and microscopic topology of entangled polymeric liquids,” *Science* **303**, 823 (2004).

¹²C. Svaneborg and R. Everaers, “Characteristic time and length scales in melts of Kremer-Grest bead-spring polymers with wormlike bending stiffness,” *Macromolecules* **53**, 1917 (2020).

¹³M. Kröger, W. Loose, and S. Hess, “Rheology and structural changes of polymer melts via nonequilibrium molecular dynamics,” *J. Rheol.* **37**, 1057 (1993).

¹⁴M. Kröger and S. Hess, “Rheological evidence for a dynamical crossover in polymer melts via nonequilibrium molecular dynamics,” *Phys. Rev. Lett.* **85**, 1128 (2000).

¹⁵M. Kröger, “Simple models for complex nonequilibrium fluids,” *Phys. Rep.* **390**, 453 (2004).

¹⁶J.-X. Hou, C. Svaneborg, R. Everaers, and G. S. Grest, “Stress relaxation in entangled polymer melts,” *Phys. Rev. Lett.* **105**, 068301 (2010).

¹⁷J. Cao and A. E. Likhtman, “Simulating startup shear of entangled polymer melts,” *ACS Macro Lett.* **4**, 1376 (2015).

¹⁸H.-P. Hsu and K. Kremer, “Static and dynamic properties of large polymer melts in equilibrium,” *J. Chem. Phys.* **144**, 154907 (2016).

¹⁹T. C. O’Connor, N. J. Alvarez, and M. O. Robbins, “Relating chain conformations to extensional stress in entangled polymer melts,” *Phys. Rev. Lett.* **121**, 047801 (2018).

²⁰W.-S. Xu, J.-M. Y. Carrillo, C. N. Lam, B. G. Sumpter, and Y. Wang, “Molecular dynamics investigation of the relaxation mechanism of entangled polymers after a large step deformation,” *ACS Macro Lett.* **7**, 190 (2018).

²¹R. Auhl, R. Everaers, G. S. Grest, K. Kremer, and S. J. Plimpton, “Equilibration of long chain polymer melts in computer simulations,” *J. Chem. Phys.* **119**, 12718 (2003).

²²R. Everaers and K. Kremer, “Test of the foundations of classical rubber elasticity,” *Macromolecules* **28**, 7291 (1995).

²³R. Everaers, “Entanglement effects in defect-free model polymer networks,” *New J. Phys.* **1**, 12 (1999).

²⁴A. Likhtman and T. McLeish, “Quantitative theory for linear dynamics of linear entangled polymers,” *Macromolecules* **35**, 6332 (2002).

²⁵C. Svaneborg, H. A. Karimi-Varzaneh, N. Hojdis, F. Fleck, and R. Everaers, “Multiscale approach to equilibrating model polymer melts,” *Phys. Rev. E* **94**, 032502 (2016).

²⁶C. Svaneborg and R. Everaers, “Multiscale equilibration of highly entangled isotropic model polymer melts.” *J. Chem. Phys.* **158**, 054903 (2023).

²⁷C. Svaneborg, “Inverse primitive path analysis,” *Comput. Phys. Commun.* **300**, 109209 (2024).

²⁸M. Mooney, “A theory of large elastic deformation,” *J. Appl. Phys.* **11**, 582 (1940).

²⁹R. S. Rivlin, “Large elastic deformations of isotropic materials iv. further developments of the general theory,” *Philos. Trans. R. Soc. A* **241**, 379–397 (1948).

³⁰R. Everaers, “Constrained fluctuation theories of rubber elasticity: General results and an exactly solvable model,” *Eur Phys. J. B* **4**, 341 (1998).

³¹B. Mergell and R. Everaers, “Tube models for rubber- elastic systems,” *Macromolecules* **34**, 5675–5686 (2001).

³²M. Warner and S. Edwards, “Neutron scattering from strained polymer networks,” *J. Phys. A: Math. Gen.* **11**, 1649 (1978).

³³G. S. Grest and K. Kremer, “Molecular dynamics simulation for polymers in the presence of a heat bath,” *Phys. Rev. A* **33**, 3628 (1986).

³⁴R. Faller, F. Müller-Plathe, and A. Heuer, “Local reorientation dynamics of semiflexible polymers in the melt,” *Macromolecules* **33**, 6602 (2000).

³⁵J. D. Weeks, D. Chandler, and H. C. Andersen, “Role of repulsive forces in determining the equilibrium structure of simple liquids,” *J. Chem. Phys.* **54**, 5237–5247 (1971).

³⁶N. Grønbech-Jensen and O. Farago, “A simple and effective Verlet-type algorithm for simulating Langevin dynamics,” *Mol. Phys.* **111**, 983 (2013).

³⁷N. Grønbech-Jensen, N. R. Hayre, and O. Farago, “Application of the G-JF discrete-time thermostat for fast and accurate molecular simulations,” *Comput. Phys. Commun.* **185**, 524 (2014).

³⁸S. Plimpton, “Fast parallel algorithms for short-range molecular dynamics,” *J. Comp. Phys.* **117**, 1 (1995).

³⁹A. P. Thompson and et al., “LAMMPS a flexible simulation tool for particle based materials modeling at the atomic, meso, and continuum scales,” *Comput. Phys. Commun.* **271**, 108171 (2022).

⁴⁰S. K. Sukumaran, G. S. Grest, K. Kremer, and R. Everaers, “Identifying the primitive path mesh in entangled polymer liquids,” *J. Polym. Sci., Part B: Polym. Phys.* **43**, 917 (2005).

⁴¹M. Mooney, “The thermodynamics of a strained elastomer. i. general analysis,” *J. Appl. Phys.* **19**, 434 (1948).

⁴²W. Kuhn, “Dependence of the average transversal on the longitudinal dimensions of statistical coils formed by chain molecules,” *J. Polym. Sci.* **1**, 380 (1946).

⁴³L. R. G. Treloar, *The physics of rubber elasticity* (Oxford University Press, USA, 1975).

⁴⁴F. T. Wall and P. J. Flory, “Statistical thermodynamics of rubber elasticity,” *J. Chem. Phys.* **19**, 1435 (1951).

⁴⁵J. E. Mark, “The constants $2c_1$ and $2c_2$ in phenomeno-logical elasticity theory and their dependence on experimental variables,” *Rubber Chem. Technol.* **48**, 495 (1975).

⁴⁶J. E. Mark, “The use of model polymer networks to elucidate molecular aspects of rubberlike elasticity,” in *Polymer Networks*, edited by K. Dušek (Springer Berlin Heidelberg,

Berlin, Heidelberg, 1982) pp. 1–26.

⁴⁷I. A. Gula, H. A. Karimi-Varzaneh, and C. Svaneborg, “Computational study of cross-link and entanglement contributions to the elastic properties of model PDMS networks,” *Macromolecules* **53**, 6907 (2020).

⁴⁸L. J. Fetter, D. J. Lohse, and R. H. Colby, “Chain dimensions and entanglement spacings,” in *Physical Properties of Polymers Handbook*, edited by J. Mark (Springer, 2007) p. 447.

⁴⁹Y. Lin, “Number of entanglement strands per cubed tube diameter, a fundamental aspect of topological universality in polymer viscoelasticity,” *Macromolecules* **20**, 3080 (1987).

⁵⁰T. A. Kavassalis and J. Noolandi, “New view of entanglements in dense polymer systems,” *Phys. Rev. Lett.* **59**, 2674 (1987).

⁵¹L. J. Fetter, D. J. Lohse, and W. W. Graessley, “Chain dimensions and entanglement spacings in dense macromolecular systems,” *J. Polym. Sci., Part B: Polym. Phys.* **37**, 1023 (1999).

⁵²R. Everaers, “Topological versus rheological entanglement length in primitive-path analysis protocols, tube models, and slip-link models,” *Phys. Rev. E* **86**, 022801 (2012).

⁵³M. Kröger, J. D. Dietz, R. S. Hoy, and C. Luap, “The Z1+ package: Shortest multiple disconnected path for the analysis of entanglements in macromolecular systems,” *Comput. Phys. Commun.* **283**, 108567 (2023).

⁵⁴D. Richter, M. Monkenbusch, A. Arbe, and J. Colmenero, *Neutron spin echo in polymer systems* (Springer, 2005) p. 1.

⁵⁵G. Zhang, L. A. Moreira, T. Stuehn, K. C. Daoulas, and K. Kremer, “Equilibration of high molecular weight polymer melts: A hierarchical strategy,” *ACS Macro. Lett.* **3**, 198 (2014).

⁵⁶G. Zhang, T. Stuehn, K. C. Daoulas, and K. Kremer, “One size fits all: Equilibrating chemically different polymer liquids through universal long-wavelength description,” *J. Chem. Phys.* **142**, 221102 (2015).

⁵⁷L. A. Moreira, G. Zhang, F. Müller, T. Stuehn, and K. Kremer, “Direct equilibration and characterization of polymer melts for computer simulations,” *Macromol. Theory Simul.* **24**, 419 (2015).

⁵⁸C. Svaneborg, G. S. Grest, and R. Everaers, “Strain-dependent localization, microscopic deformations, and macroscopic normal tensions in model polymer networks,” *Phys. Rev.*

Lett. **93**, 257801 (2004).

⁵⁹C. Svaneborg, R. Everaers, G. S. Grest, and J. G. Curro, “Connectivity and entanglement stress contributions in strained polymer networks,” *Macromolecules* **41**, 4920 (2008).

⁶⁰C. Svaneborg and R. Everaers, “Equilibrated Kremer-Grest polymer melts of M=500 linear chains with Z=100 entanglements for varying chain stiffness.” (2023).

⁶¹C. Svaneborg and R. Everaers, “Equilibrated Kremer-Grest polymer melts of M=1000 linear chains with Z=200 entanglements for varying chain stiffness.” (2023).

⁶²C. Svaneborg, “Inverse Primitive Path Analysis (IPPA) package for LAMMPS. Zenodo: doi:10.5281/zenodo.10952427 and Github: <https://github.com/zqex/iPPA>,” (2024).